



# Efficient utilization of nickel single atoms for CO<sub>2</sub> electroreduction by constructing 3D interconnected nitrogen-doped carbon tube network

Kui Wang<sup>a,1</sup>, Bin Chen<sup>b,1</sup>, Yimin Xuan<sup>a,\*</sup>, Wenjun Fan<sup>c</sup>, Nan Sun<sup>a</sup>, Sheng Chang<sup>a</sup>, Guowen Meng<sup>b</sup>

<sup>a</sup> School of Energy and Power Engineering, Nanjing University of Aeronautics and Astronautics, Nanjing 210016, China

<sup>b</sup> Key Laboratory of Materials Physics and Anhui Key Laboratory of Nanomaterials and Nanotechnology, Institute of Solid State Physics, HFIPS, Chinese Academy of Sciences, Hefei 230031, China

<sup>c</sup> State Key Laboratory of Catalysis, Dalian National Laboratory for Clean Energy, Dalian Institute of Chemical Physics, Chinese Academy of Sciences, Dalian 116023, China

## ARTICLE INFO

### Keywords:

CO<sub>2</sub> electroreduction  
Single-atom catalysts  
N-doped carbon tube network  
Ni-N<sub>4</sub>  
Self-supported electrode

## ABSTRACT

The CO<sub>2</sub> electroreduction (CO<sub>2</sub>RR) is extensively deemed as a promising route to reach carbon neutralization, while the single-atom catalysts (SACs) are proved to be effective in CO<sub>2</sub>RR. However, most SACs cannot further amplify performance due to their powdery feature. Herein, we present numerous isolated nickel single atoms anchored on 3D interconnected N-doped carbon tubes (NiSAs@3D-INCT) network as a self-supported electrode. The NiSAs@3D-INCT has truly interconnected and highly ordered vertical and lateral carbon tube-channels, which promote the CO<sub>2</sub> interaction and electrolyte transmission. The NiSAs@3D-INCT exhibits a superior CO<sub>2</sub>RR performance with an appreciable CO partial current density of 51.8 mA cm<sup>-2</sup> at -0.96 V versus the reversible hydrogen electrode (RHE). X-ray absorption fine structure spectroscopy and theoretical computations reveal the NiSAs are loaded on the 3D-INCT network with Ni-N<sub>4</sub> configuration as highly active sites for CO<sub>2</sub>RR. This work will shed a new light on opening up high performance SACs for CO<sub>2</sub>RR.

## 1. Introduction

The global climatic change resulted from substantially increased atmospheric CO<sub>2</sub> concentrations has urgently menaced the sustainable development of human society [1–5]. CO<sub>2</sub> electroreduction (CO<sub>2</sub>RR) can store intermittent renewable electric energy in the form of chemical bonds and has been regarded as an encouraging strategy to close the carbon cycle and achieve carbon neutrality [6,7]. Through different strategies, CO<sub>2</sub> can be reduced to CO, HCOO<sup>-</sup>, CH<sub>3</sub>OH, CH<sub>4</sub>, C<sub>2</sub>H<sub>4</sub>, etc [8–15]. Among them, CO has attracted much attention, because it can be easily added to the production procedures of the chemical industries through the Fischer-Tropsch reaction with high technoeconomic superiority [6,16–18]. Up to now, noble metals such as Au, Ag and their alloys have been considered as the most effective CO<sub>2</sub>RR catalysts, especially at low overpotential, but the excessive cost has greatly obstructed their practical applications [19–21]. Transition metal-based catalysts have attracted increasing attention due to their low expenditure and earth abundance. However, the conventional transition

metal-based nanoparticles (NPs) are not suitable for CO<sub>2</sub>RR owing to the serious competitive reaction. Recently, transitional metal single-atom catalysts (SACs) are expected to achieve significantly improved catalytic activity and selectivity for CO<sub>2</sub>RR because of their unsaturated coordination configuration and special electronic structure, as well as the advantages of maximizing the atomic utilization rate of homogeneous catalysts [22–26].

Among various transition metal SACs, Ni-SACs have been valued as productive CO<sub>2</sub>RR electrocatalysts assignable to their special virtue in commensurate selectivity and intrinsic activity with noble metals. For instance, Jiang et al. found that anchoring Ni-N<sub>3</sub> sites on deeply defective hierarchical carbon was favorable for electron transport and exposure of active sites, and thus boosting CO<sub>2</sub>RR performance [27]. Lou et al. developed a Ni-templated method to enhance charge / mass transfer and exposure of active sites by converting metal Ni into Ni single atoms (NiSAs) loaded on hollow porous N-doped carbon [28]. Jiang et al. prepared Ni-SACs with different N coordination numbers on N-doped carbon and found that the lower Ni coordination number of

\* Corresponding author.

E-mail address: [ymxuan@nuaa.edu.cn](mailto:ymxuan@nuaa.edu.cn) (Y. Xuan).

<sup>1</sup> These authors contributed equally to this work

Ni-N<sub>3</sub>-C catalysts can contribute to the formation of COOH\* and thus accelerate CO<sub>2</sub>RR [29]. Despite the fact that great advancements have been made in improving CO<sub>2</sub>RR activity by designing unique support structures and adjusting the coordination environment of NiSAs, most of the previously reported catalysts were usually prepared in the powder form [30–32], and must be fixed on the conductive substrates by means of polymer binders, such as Nafion or PVDF, which would lead to a decrease in the charge transfer and a reduction in the exposure of active sites to a large extent [33,34]. And the detachment of the powdery SACs during the reaction will trade off the stability and raise the cost, which seriously limit the practical application [35,36]. In addition, the lack of directional designing the structure of substrates that assists mass and charge transport also reduces the scalability of upgrade CO<sub>2</sub>RR performance in large current density.

Herein, we propose an extensible approach to obtain self-supported Ni-SACs electrode by anchoring isolated NiSAs on a three-dimensionally (3D) interconnected vertical and lateral N-doped carbon tube (3D-INCT) network (denoted as NiSAs@3D-INCT) via a unique 3D nanoporous anodic aluminum oxide (3D-AAO) template assisted method. As a free-standing and ordered network support, the 3D-INCT with large surface area has abundant defects to assist the anchoring of NiSAs, and the unique structural characteristics of the interconnected channels and hierarchical opening pores tremendously facilitate the accessibility of Ni-N<sub>4</sub> sites and effectively obtain excellent mass and charge transfer capability, polishing up the activity and selectivity for CO<sub>2</sub>RR. As a result, the NiSAs@ 3D-INCT electrode exhibits an ultrahigh CO partial current density of 51.5 mA cm<sup>-2</sup> at -0.96 V versus the reversible hydrogen electrode (RHE), and acquires the peak Faraday efficiency for CO production (FE<sub>CO</sub>) of 91.4% at -0.86 V vs. RHE in the H-type cell. Moreover, the NiSAs@ 3D-INCT displays a robust stability of current density and selectivity in 12 h of uninterrupted operation. X-ray absorption fine structure spectroscopy (XAFS) and density functional theory (DFT) calculations further manifest that the atomic configuration of Ni-N<sub>4</sub> in NiSAs@ 3D-INCT profits the production of CO.

## 2. Experimental

### 2.1. Chemicals and materials

Nickel nitrate hexahydrate (Ni(NO<sub>3</sub>)<sub>2</sub>•6 H<sub>2</sub>O), nitric acid (HNO<sub>3</sub>) and hydrofluoric acid (HF) were acquired from Aladdin Biochemical Technology Co. Ltd, Shanghai, China. Phosphoric acid (H<sub>3</sub>PO<sub>4</sub>), hydrochloric acid (HCl), sulfuric acid (H<sub>2</sub>SO<sub>4</sub>), ethanol (C<sub>2</sub>H<sub>6</sub>O), tin chloride pentahydrate (SnCl<sub>4</sub>•5H<sub>2</sub>O), and potassium bicarbonate (KHCO<sub>3</sub>) were purchased from Sinopharm Chemical Reagent Co. Ltd, China. The Aluminum (Al) foils with Cu impurity was obtained from Shanghai Dingxin Materials Co. Ltd, China. The Nafion 117 membrane was obtained from SCI Materials Hub. Ultrapure water (18.2 MΩ cm) was provided by Milli-Q ultrapure water system. All chemicals were used without further purification.

### 2.2. Material synthesis

Firstly, the 3D-AAO template was prepared by the anodization of Al foil with impurity at 195 V for 20 h in a 0.3 M H<sub>3</sub>PO<sub>4</sub> mixed solution (H<sub>2</sub>O: C<sub>2</sub>H<sub>6</sub>O = 9:1 (v: v)) at 5 °C (see more details in the [Supporting Information](#) and our previous work) [37]. Next, the 3D-AAO template was put into a tubular furnace for chemical vapor deposition (CVD) under 6 sccm acetylene (C<sub>2</sub>H<sub>2</sub>), 20 sccm ammonia (NH<sub>3</sub>) and 60 sccm argon (Ar) at 900 °C. After 90 min of deposition, the supply of C<sub>2</sub>H<sub>2</sub> and NH<sub>3</sub> was turned off, and the furnace was cooled to room temperature under flowing Ar. The 3D-AAO template was removed after treatment in HF for 48 h at room temperature, and the 3D-INCT film was obtained after rinsing in ultrapure water. As a control experiment, the pure 3D-INCT film without N-dopant was prepared by the same procedure of 3D-INCT without adding NH<sub>3</sub> gas during the CVD process.

The 3D-INCT was treated by plasma cleaning on both sides to obtain the two-end opening structure, and then immersed in a mixed solution of 30 mL 98% H<sub>2</sub>SO<sub>4</sub> and 10 mL 68% HNO<sub>3</sub> at 60 °C for 2 h to obtain activated 3D-INCT. After activation, the 3D-INCT was immersed in 0.02 M Ni(NO<sub>3</sub>)<sub>2</sub> solution and vacuumized, and then transferred to an oven at 40 °C for 3 h to absorb the Ni<sup>2+</sup>. After rinsing with ultrapure water to remove the Ni<sup>2+</sup> residue, the Ni<sup>2+</sup> decorated 3D-INCT was dried in air and then annealed at 800 °C for 1 h under 60 sccm Ar with a heating rate of 5 °C min<sup>-1</sup>. Finally, the as-treated product was soaked in 3 M HCl at 80 °C overnight to remove the Ni nanoparticles (NiNPs), and the resultant product was referred to as NiSAs@ 3D-INCT. As a control sample, the NiNPs@ 3D-INCT was synthesized under the same process as NiSAs@ 3D-INCT without HCl leaching. In addition, the 3D-INCT networks were immersed in the impregnation Ni(NO<sub>3</sub>)<sub>2</sub> solution with varied concentrations of 0.05 M and 0.5 M, respectively, to control the loading NiSAs content and optimize the catalytic performance.

### 2.3. Material characterization

The morphologies of all catalysts were acquired via scanning electron microscopy (SEM, Zeiss GeminiSEM 300 and Hitachi SU8020) and transmission electron microscopy (TEM, FEI Tecnai G2 F20 equipped with energy-dispersive X-ray spectroscopy (Oxford EDS)). The distributions of Ni single atoms were observed by the high-angle annular dark-field scanning transmission electron microscope with a spherical aberration corrector (AC-HAADF-STEM JEOL JEM-ARM200F). X-ray diffraction (XRD) patterns were measured on a PANalytical X'pert-PRO MPD with Cu Kα radiation. Raman spectra were attained on a confocal microscopic Raman spectrometer (Renishaw inVia Reflex). The metal contents in the catalysts were measured by inductively coupled plasma mass spectrometry ICP-MS (Thermo Scientific iCAP Qc). Brunauer-Emmett-Teller (BET) method was applied to measure the specific surface area of the sample (Micromeritics, ASAP 2460). The FTIR spectra of samples were received by Thermo SCIENTIFIC (iS50 FT-IR). The element composition and status were recorded by X-ray photoelectron spectroscopy (XPS, Thermo Scientific ESCALAB 250 Xi spectrometer Al Kα). XAFS at Ni K-edge were performed on 1W1B beamline of Beijing Synchrotron Radiation Facility (BSRF). The data of sample were acquired in fluorescence mode using a Lytle detector and the corresponding reference samples were obtained in transmission mode. The collected XAFS data were carried out depending on the standard procedures using the ATHENA module of Demeter software packages [38]. The quantitative structural parameters around central atoms were obtained by fitting the least-squares curve parameter using the ARTEMIS module of Demeter software packages.

### 2.4. Electrochemical CO<sub>2</sub>RR activity measurements

CO<sub>2</sub>RR performance was estimated by an electrochemical workstation (CHI 660E, CH Instruments Co., China) in a sealed H-type cell with two chambers contained CO<sub>2</sub> saturated 0.5 M KHCO<sub>3</sub> electrolyte (pH = 7.2). Pt sheet and Ag/AgCl (3 M KCl) served as the counter and reference electrodes, respectively. The self-supported electrodes synthesized by different processes were cut into pieces with an area of 1 × 1 cm<sup>2</sup>, and were nipped on the glassy carbon clamp as the working electrode. The anode and cathode chambers were separated by Nafion 117 membrane. All the potentials measured after 90% iR compensation were calibrated to RHE on the basis of the Nernst equation ( $E_{(RHE)} = E_{(Ag/AgCl)} + 0.0591 \times pH + 0.197$  V). The KHCO<sub>3</sub> solution was purged with CO<sub>2</sub> for 45 min before the measurements, and the flow rate of CO<sub>2</sub> was maintained at 20 sccm during the tests. LSV was performed with a scan rate of 5 mV s<sup>-1</sup>. The CO<sub>2</sub>RR performance of electrode under different potentials was evaluated by chronoamperometry. The EIS was performed in a frequency range from 0.01 Hz to 1 MHz at a voltage amplitude of 5 mV under open circuit potential by a Zahner Zennium pro electrochemical workstation. The Tafel slope was calculated based on the Tafel equation

( $\eta = b \log(j_{\text{CO}}/j^0)$ ), where  $\eta$  is the overpotential,  $b$  is the Tafel slope,  $j_{\text{CO}}$  is the partial current density of CO, and  $j^0$  is the exchange current density.

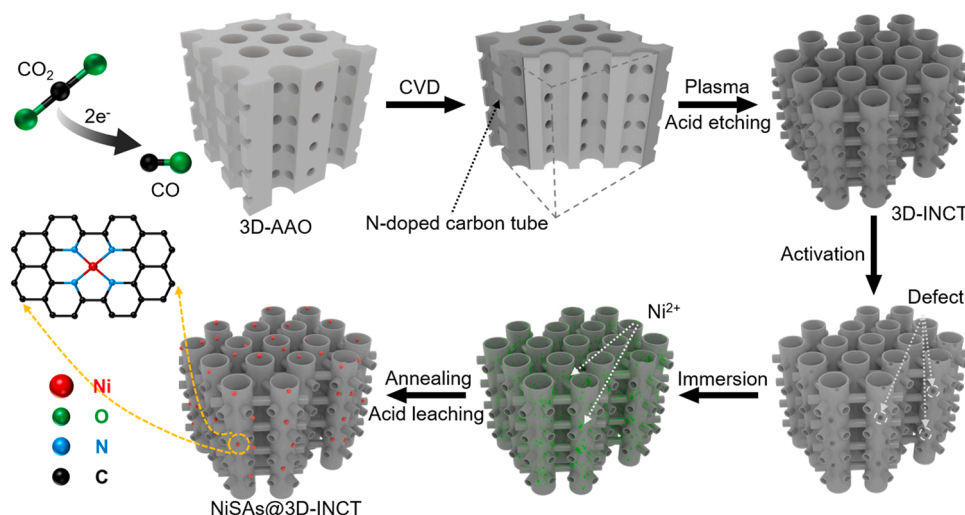
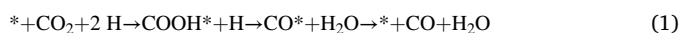
The working electrode was kept at a constant potential for 15 min when testing the CO<sub>2</sub>RR performance and corresponding products, and the gas products were detected by an online gas chromatography (GC, A91 Plus, PANNA) used Ar as the carrier gas and equipped with a thermal conductivity detector (TCD) and flame ionization detector (FID) when the electrolysis process runs for 10 min. During the stability test, the products were examined by GC every 30 min. Liquid products were analyzed by Bruker AVIII 500 MHz NMR spectroscopy.

The FE of the specific product was calculated by  $FE_{\text{product}} = zFn_{\text{product}} / It$ , where  $z$  is the number of transfer electrons, which is 2 for both H<sub>2</sub> and CO,  $F$  is the faraday constant (96485 C mol<sup>-1</sup>),  $n$  is the total amount of products according to the standard curves of GC,  $I$  is the average test current at a specific applied potential during a fixed time ( $t$ ).

## 2.5. DFT calculation details

Our theoretical calculations were carried out with the use of the Perdew-Burke-Ernzerhof (PBE) of Generalized Gradient Approximation (GGA) within the framework of density functional theory (DFT) methods with the pseudo-potential plane wave, which were implemented on VASP (Vienna *ab initio* simulation package) [39–41]. The plane-wave cut-off energy and the convergence criterion for the energy per atom were set to be 500 eV and 10<sup>-5</sup> eV respectively, and the convergence criterion for calculating the force was until the force per atom is less than 0.02 eV/Å. The Brillouin zone sampling was adopted using a Monkhorst-Pack grid 3 × 3 × 1. Solvation effects were not considered in the calculations. For the NiSAs@3D-INCT, according to the fitting results of EXAFS, we employed the 5 × 5 × 1 supercell of nickel- and nitrogen-doped graphene, where one Ni atom and four N atoms form coordination. For the 3D-INCT, we also adopted the 5 × 5 × 1 supercell of a nitrogen-doped graphene in which one C atom was replaced by a N atom and a neighboring C atom was removed. The vacuum layer larger than 15 Å was set along the z direction.

The adsorption energy was calculated by  $E_a = E_{\text{final}} - E_{\text{substrate}} - E_{\text{adsorbate}}$ , where  $E_a$ ,  $E_{\text{final}}$ ,  $E_{\text{substrate}}$  and  $E_{\text{adsorbate}}$  are the adsorption energy of adsorbate on substrate, total energy of adsorbate on this substrate, total energy of substrate and total energy of adsorbate, respectively. The involved reaction mechanisms of CO<sub>2</sub>RR and HER are as follows [42]:



**Scheme 1.** Schematic illustration of the synthesis of free-standing NiSAs@3D-INCT.

The Gibbs free energy of a species was calculated by following equation [43]:

$$\Delta G = E_a + \Delta \text{ZPE} - T\Delta S$$

where  $\Delta G$ ,  $\Delta \text{ZPE}$  and  $\Delta S$  represent Gibbs free energy, zero point energy and the entropy, respectively.

## 3. Results and discussion

### 3.1. Materials preparation and characterization

The synthesis procedures of NiSAs@3D-INCT are shown in Scheme 1. The 3D-AAO templates with interconnected vertical and lateral nano-channels (Fig. S1 and S2) were prepared by the anodization of Al foils with Cu-impurities where Cu-contained NPs were embedded in the channel walls and selectively etched in phosphoric acid solutions [37]. The 3D-INCT was synthesized in the 3D-AAO template by CVD process with C<sub>2</sub>H<sub>2</sub> and NH<sub>3</sub> gas as C and N sources, and the 3D interconnected carbon tube (3D-ICT) without N-dopant was similarly obtained except NH<sub>3</sub> flowing. After removing the AAO template, both the self-supported 3D-INCT and 3D-ICT films have interconnected nanotubes which inherited from the 3D-AAO templates (Fig. S3). The thicknesses of 3D-INCT films can be regulated by adjusting the anodization duration of the 3D-AAO templates (Fig. S4). To sufficiently adsorb and anchor Ni<sup>2+</sup>, the 3D-INCT was treated and activated in concentrated a mixture of H<sub>2</sub>SO<sub>4</sub> and HNO<sub>3</sub> [34,44–46]. Fig. S5a demonstrates that a large amount of oxygen-containing functional groups including –OH and C=O were introduced during the activation treatment process. Raman spectrum (Fig. S5b) displays two characteristic peaks located at 1362 and 1577 cm<sup>-1</sup> which are assigned to D and G band of carbon materials, respectively. The 3D-INCT after the activation treatment has a higher relative intensity ratio of D to G bands ( $I_D/I_G = 1.070$ ) than that of the initial 3D-INCT ( $I_D/I_G = 0.986$ ), indicating that the activation treatment brings more defects. The typical NiSAs@3D-INCT was attained by immersion of 3D-INCT in 0.2 M Ni(NO<sub>3</sub>)<sub>2</sub>, pyrolysis and HCl leaching to remove excess NiNPs, and the atomically dispersed Ni sites were expected to be anchored on the defects originated from nitridation and activation.

Fig. 1 shows morphology and structure characterizations of the typical NiSAs@3D-INCT obtained in 0.2 M Ni(NO<sub>3</sub>)<sub>2</sub> solution. The free-standing NiSAs@3D-INCT network with the size of 2.5 × 2.5 cm<sup>2</sup> (Fig. 1a) can be cut into a specific size as a self-supported electrode for CO<sub>2</sub>RR. The inset of Fig. 1a shows that the obtained film has good flexibility. The SEM images reveal that the morphology of the 3D-INCT substrate can be entirely kept after the introduction of Ni species



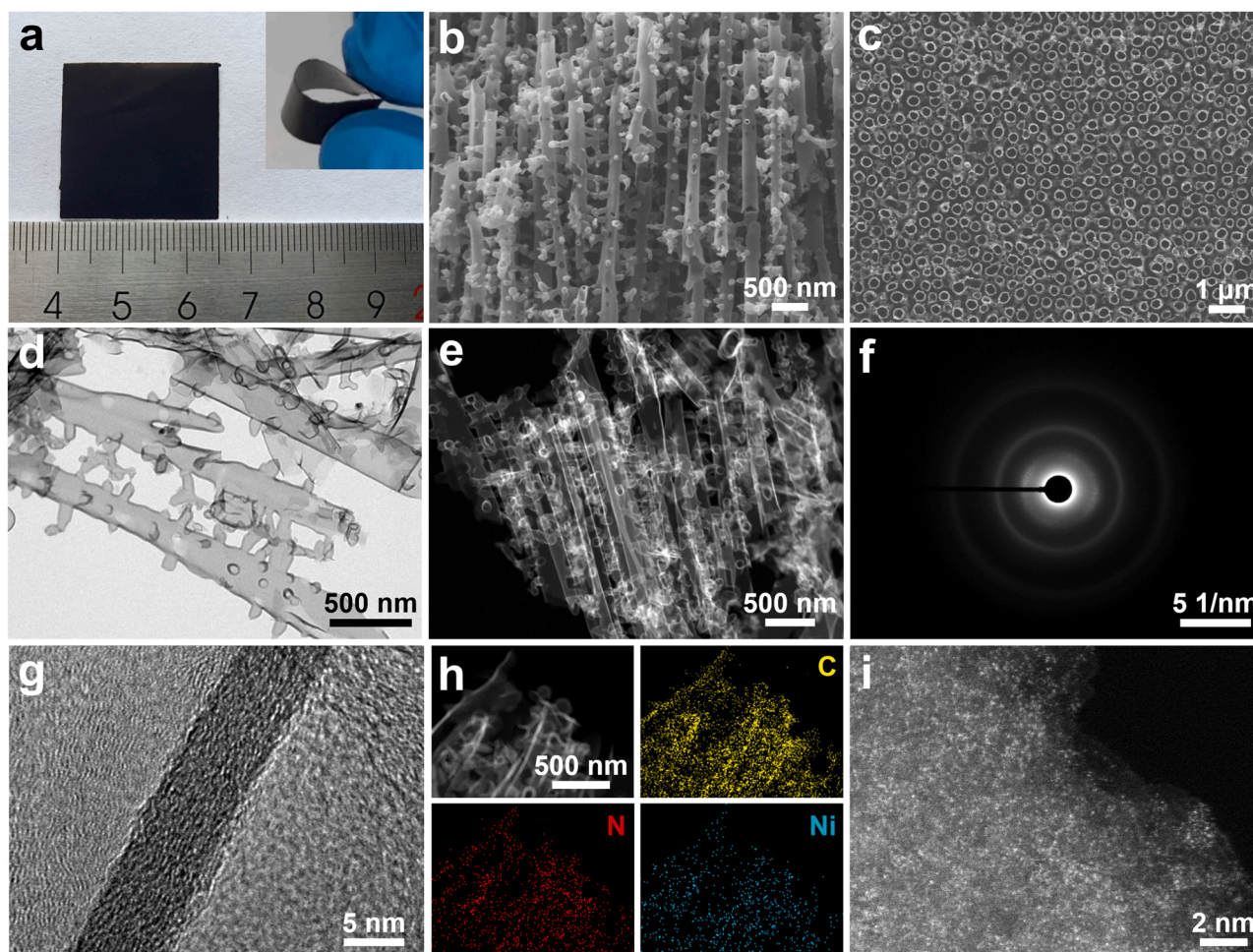


**Fig. 1.** Characterizations of the NiSAs@ 3D-INCT obtained in 0.2 M Ni ( $\text{NO}_3$ )<sub>2</sub> solution. a) Photograph. b) Cross-sectional and c) top-view SEM images. d) TEM, e) STEM, f) SAED and g) HRTEM images. h) HAADF-STEM image and the corresponding EDS mappings. i) AC-HAADF-STEM image. (Massive and dispersive bright dots are related with the heavier Ni elements and referred to Ni atoms).

(Fig. 1b, c and Fig. S6a). The vertical carbon tubes (CTs) are aligned and interconnected with the lateral CTs to form 3D CTs network. The NiSAs@3D-INCT film has uniform thickness of 30  $\mu\text{m}$  with diameters of 180 nm and 87 nm for vertical and lateral CTs, respectively (Fig. S6b-d). The TEM and the HAADF-STEM observations further confirm the truly interconnected structure of NiSAs@3D-INCT (Fig. 1d, e). No visible NiNPs can be found in both SEM and TEM images, indicating that the NiNPs were completely removed. In addition, the selected area electron diffraction (SAED) pattern (Fig. 1f) shows only the characteristic diffraction of carbon, further ruling out the existence of NiNPs. The typical lattice fringes of layered carbon matrix in high-resolution TEM (HRTEM) image (Fig. 1g) indicate that the obtained 3D-INCT network possesses a good crystallinity, which would effectively improve the electronic conductivity [47]. STEM image and the corresponding elemental mappings indicate the presence of C, N and Ni elements which are uniformly distributed all through the substrate (Fig. 1h). As shown in Fig. 1i and Fig. S7, the HAADF-STEM with a spherical aberration corrector (AC-HAADF-STEM) images reveal that an ultrahigh density of isolated Ni atoms are homogeneously distributed throughout the NiSAs@3D-INCT, and no obvious existences of metal NPs over a large area in the matrix. As a contrast, NiNPs were obviously distributed in NiNPs@3D-INCT (Fig. S8).

The XRD pattern of NiSAs@ 3D-INCT network shows two broad diffraction peaks at  $26.2^\circ$  and  $44.4^\circ$  attributed to the (002) and (101) crystal planes of graphite carbon respectively (Fig. 2a), consistent with the SAED and HRTEM analyses [48]. Besides, there was no characteristic

diffraction peaks corresponding to Ni species in the XRD pattern, further demonstrating that the Ni species are dispersed atomically. As shown in Fig. S9, the 3D-INCT has a higher relative intensity ratio of D to G bands ( $I_D/I_G = 0.986$ ) than that of the pure 3D-INCT ( $I_D/I_G = 0.975$ ), indicating that the N-doping yields highly defective carbon. After decorating Ni species, the relative intensity ratio of D to G bands shows no obvious changes for both NiSAs@3D-INCT ( $I_D/I_G = 0.982$ ) and NiNPs@3D-INCT ( $I_D/I_G = 0.986$ ) [33]. The Ni content in NiSAs@ 3D-INCT is 3.62 wt% in the light of the ICP-MS detection. As there are almost no metal NPs, it further confirms that the NiSAs are dispersed densely, coinciding well with the AC-HAADF-STEM images. The NiSAs@3D-INCT network exhibits a large specific surface area of 96.22  $\text{m}^2/\text{g}$ , and the hysteresis loop type indicates the existence of mesopores and macropores in the NiSAs@3D-INCT network (Fig. S10), which is consistent with the characterization results of SEM and TEM.

The element composition of NiSAs@3D-INCT network can be further indicated by XPS survey spectrum (Fig. S11a and Table S1). The high-resolution C 1s spectrum of 3D-INCT could be deconvoluted into three peaks at 284.8 eV (C-C), 285.8 eV (C-N) and 289.2 eV (C-O), further indicating that the N species were successfully doped into the carbon matrix (Fig. S11b and Fig. S12a,c) [49]. The N 1s spectrum of 3D-INCT could be fitted into four typical peaks corresponding to oxidized N (402.8 eV), graphitic N (401.1 eV), pyrrolic N (400.3 eV) and pyridinic N (398.2 eV), respectively (Fig. S12b). The N species could contribute abundant anchoring sites to stabilizing the Ni centers. After decorating the NiSAs, there is a new peak at 399.0 eV in the N 1s

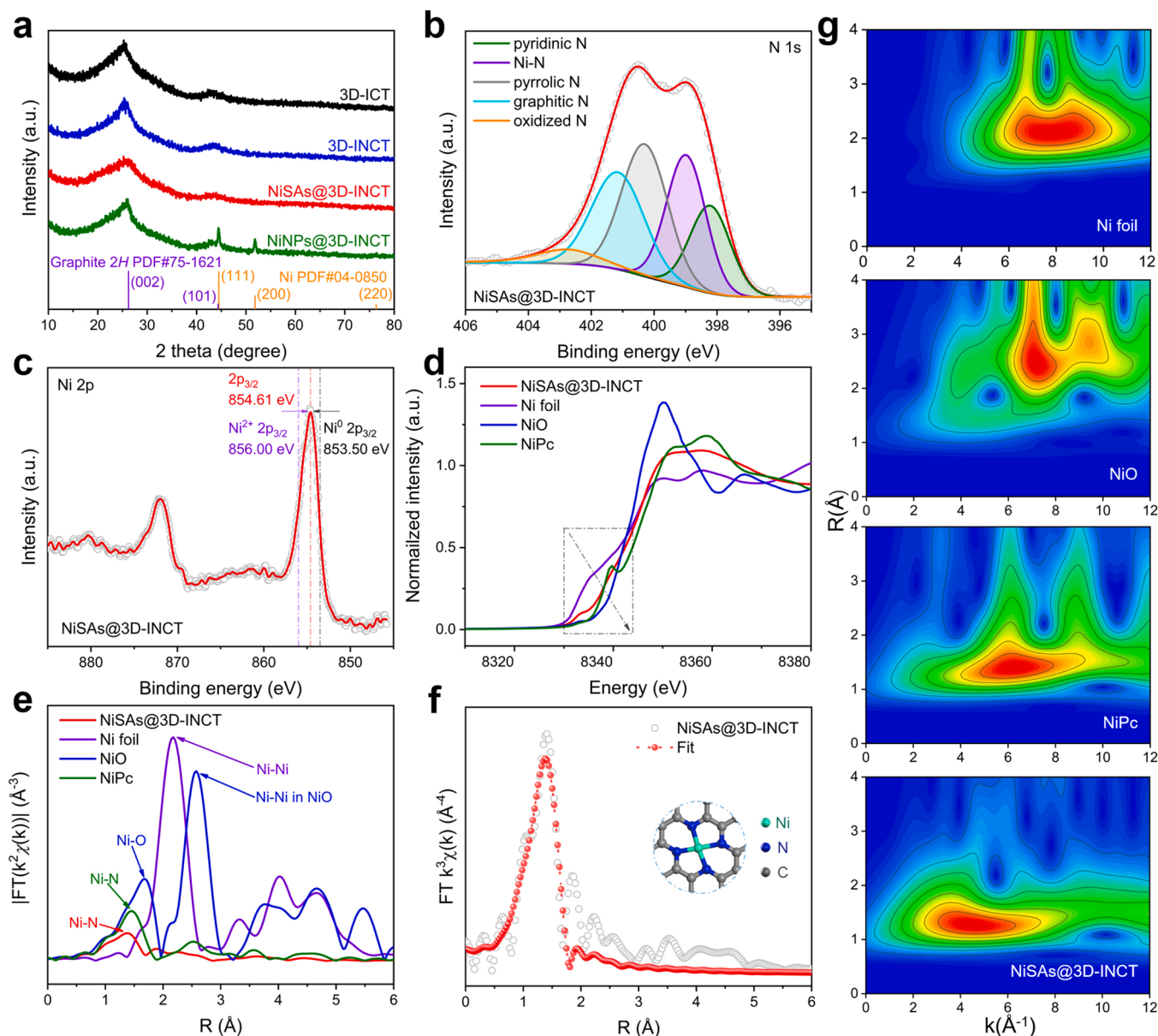


**Fig. 2.** a) XRD patterns of 3D-ICT, 3D-INCT, NiSAs@3D-INCT and NiNPs@3D-INCT. b) N 1s and c) Ni 2p high-resolution XPS spectra of NiSAs@3D-INCT. d) Ni K-edge XANES spectra of NiSAs@3D-INCT and references including Ni foil, NiO and NiPc. e) Fourier transformed curves of Ni K-edge EXAFS spectra. f) Ni K-edge EXAFS fitting result of NiSAs@3D-INCT, and the inset shows the proposed coordination configuration of the Ni center. g) WT-EXAFS contour patterns of Ni foil, NiO, NiPc and NiSAs@3D-INCT.

spectrum of NiSAs@3D-INCT, which could be assigned to the bonding between N and Ni sites, demonstrating that the Ni species with the form of Ni-N<sub>x</sub> coordination are atomically dispersed throughout the entire substrate (Fig. 2b and Table S2) [50]. As depicted in the Ni 2p spectrum of NiSAs@3D-INCT, the peak at 854.61 eV (Ni 2p<sub>3/2</sub>) is lower than that of Ni<sup>2+</sup> (Ni 2p<sub>3/2</sub>: 856.0 eV), but higher than that of Ni<sup>0</sup> (Ni 2p<sub>3/2</sub>: 853.5 eV), indicating the existence of Ni<sup>δ+</sup> centers (0 < δ < 2) in NiSAs@3D-INCT (Fig. 2c) [51].

To support the above discussions, we systematically studied the local coordination environment of Ni atoms by synchrotron radiation XAFS. In Fig. 2d, the Ni K-edge X-ray absorption near edge structure (XANES) spectra show that the absorption energy threshold for NiSAs@3D-INCT is located between NiO and Ni foil reference samples, and close to that of nickel phthalocyanine (NiPc). These results further demonstrate that the Ni species are in a low oxidation state between 0 and + 2, in accordance with the XPS analyses [47]. Fourier transform *k*<sup>2</sup>-weighted extend XAFS spectra (FT-EXAFS) were further obtained to better reveal the possible

atomic structure of NiSAs. It can be notably seen in the Fig. 2e that only one peak exists at 1.39 Å assigned to the Ni-N scattering path for the NiSAs@ 3D-INCT [28]. The peak related to the Ni-Ni interaction (2.18 Å) in Ni foil is not obviously observed in the FT-EXAFS of the NiSAs@3D-INCT, further confirming the uniformly atomic distributions of Ni atoms, and coinciding well with the AC-HAADF-STEM images and XRD analyses. The fitting results of EXAFS show the coordination number of Ni atoms with N atoms is 4 (Fig. 2f, Fig. S13-S14 and Table S3), indicating that the NiSAs@ 3D-INCT owns the atomic coordination structure of Ni-N<sub>4</sub> moiety (inset of Fig. 2f). In addition, wavelet transform (WT) analyses of EXAFS (WT-EXAFS) could be used to further infer the discrete Ni species of NiSAs@3D-INCT. As shown in Fig. 2g, comparing with Ni foil, NiO and NiPc, the WT-EXAFS contour pattern of NiSAs@3D-INCT shows the maximum intensity at around 4.4 Å<sup>-1</sup>, attributable to the Ni-N pairs. There is no intensity maximum located at 7.2 Å<sup>-1</sup> of Ni-O pairs and 7.9 Å<sup>-1</sup> of Ni-Ni pairs observed for NiSAs@3D-INCT, further supporting its single atoms feature [52]. Based



on all the above characterizations and analyses, a high density of isolated NiSAs have been successfully loaded on the 3D-INCT network with vertically and laterally interconnected channels by the atomic configuration of Ni-N<sub>4</sub>.

### 3.2. Electrochemical CO<sub>2</sub> reduction measurement

The as-prepared samples were directly worked as self-supported electrodes nipped on the glassy carbon electrode clamp for the CO<sub>2</sub>RR. The CO<sub>2</sub>RR performances were measured in CO<sub>2</sub>-saturated 0.5 M KHCO<sub>3</sub> using a sealed H-type cell separated by a Nafion 117 membrane. As illustrated in Fig. S15, the linear sweep voltammetry (LSV) profiles show that the current density of NiSAs@3D-INCT rises rapidly with the increase of applied potential, and presents much higher current response

than those of NiNPs@3D-INCT, 3D-INCT and 3D-ICT. Specifically, it is obvious that the NiSAs@3D-INCT shows a much more positive onset potential than those of NiNPs@ 3D-INCT, 3D-INCT and 3D-ICT, which can be attributed to the dense dispersion of atomic Ni-N<sub>4</sub> sites. To better evaluate the CO<sub>2</sub>RR performance and clarify the products distribution, the chronoamperometry profiles under different potentials on these electrodes were obtained, and the gas and liquid products were quantified by online gas chromatography (GC) and NMR, respectively. The steady-state polarization curves calculated by the average current densities in a specific duration demonstrate the same tendency with LSV profiles (Fig. 3a, Fig. S16). Only CO and H<sub>2</sub> were detected (Fig. S17), and the corresponding Faraday efficiencies (FEs) are shown in Fig. 3b and Fig. S18. The NiSAs@3D-INCT exhibits a high CO FE (FE<sub>CO</sub>) > 80% in the relatively broad potential window from -0.7 to -1.0 V vs. RHE,

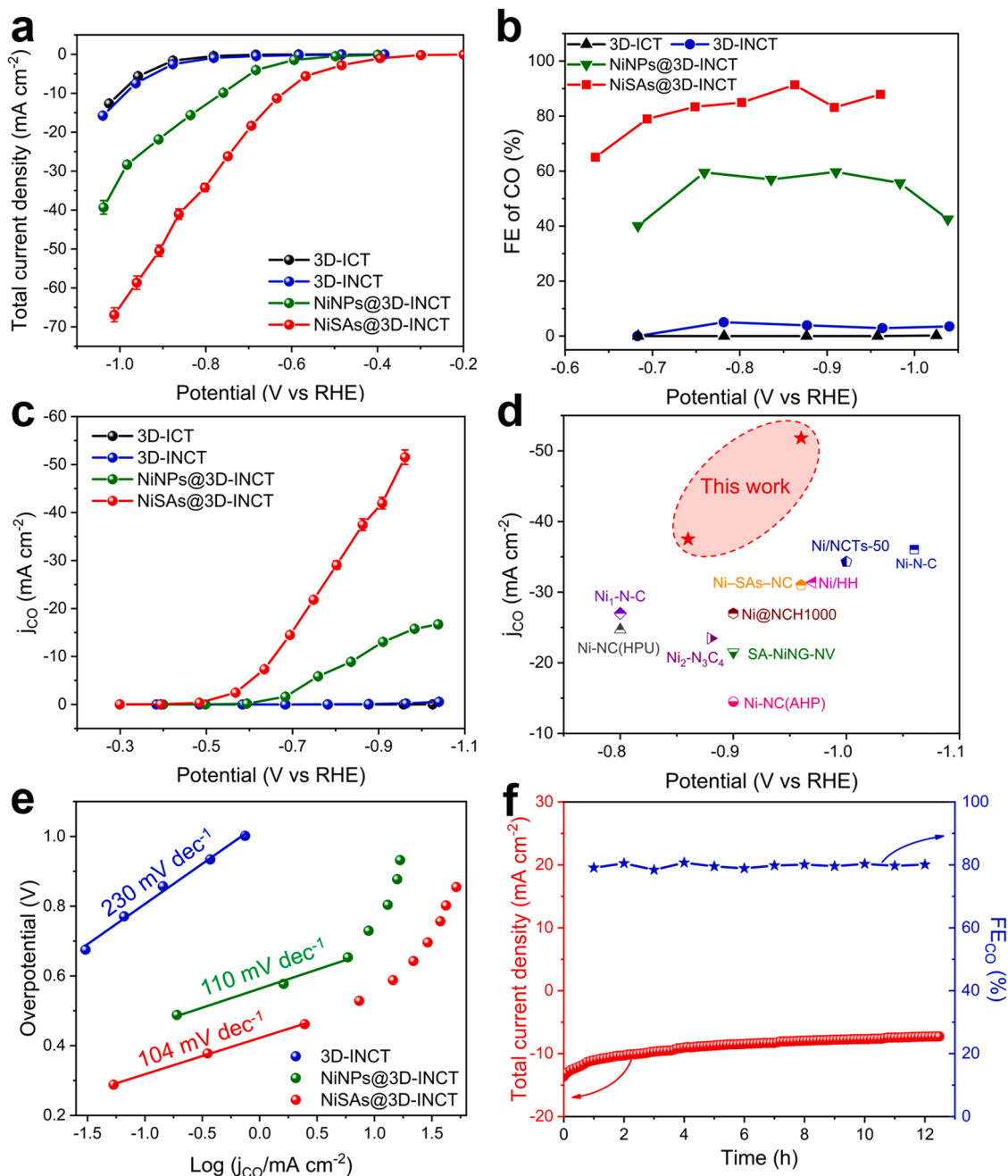


**Fig. 3.** a) Steady-state polarization curves and b) FE<sub>CO</sub> at various applied potentials for different electrodes of 3D-ICT, 3D-INCT, NiNPs@3D-INCT and NiSAs@3D-INCT, respectively. The j<sub>CO</sub> of NiSAs@3D-INCT in comparison with c) NiNPs@3D-INCT, 3D-INCT and 3D-ICT and d) representative CO<sub>2</sub>RR catalysts recently reported. e) Tafel slope plots of different electrodes towards CO product. f) Long-term stability measurement of NiSAs@3D-INCT for CO<sub>2</sub>RR at -0.69 V vs. RHE.

and has a maximum  $FE_{CO}$  of 91.4% at  $-0.86$  V vs. RHE. Quite the opposite, the 3D-INCT and 3D-ICT own a maximum  $FE_{CO}$  of 5.1% ( $-0.78$  V vs. RHE) and only 0.3% ( $-1.03$  V vs. RHE) respectively, and both of them show much lower  $FE_{CO}$  than those of NiSAs@3D-INCT at all potentials. Besides, the  $FE_{CO}$  of NiNPs@3D-INCT is lower than that of NiSAs@3D-INCT throughout the applied potentials, which is because the NiNPs sites occupy the accessibility of the Ni-N<sub>4</sub> active sites and thus bring about a competitive reaction. Meanwhile, NiSAs@3D-INCT performs a partial current density towards CO ( $j_{CO}$ ) of  $37.5 \text{ mA cm}^{-2}$  along with a  $FE_{CO}$  of 91.4% at  $-0.86$  V vs. RHE, which outperforms NiNPs@3D-INCT, 3D-INCT, 3D-ICT and most of the recently reported catalysts in H-type cell (Fig. 3c, d and Table S4) [28,30,47,53–59]. Notably, the  $j_{CO}$  of NiSAs@3D-INCT can be further enlarged to  $51.8 \text{ mA cm}^{-2}$  at  $-0.96$  V vs. RHE with an insignificant drop in  $FE_{CO}$  from 91.4% to 87.9%.

To acquire the accessible surface area during the electroreduction process, the electrochemical active surface areas (ECSAs) of the as-prepared electrodes were evaluated using the double-layer capacitance ( $C_{dl}$ ) (Fig. S19, see more details in the Supporting Information). The NiSAs@3D-INCT shows a higher ECSA of  $28.3 \text{ mF cm}^{-2}$  than those of NiNPs@3D-INCT ( $18.45 \text{ mF cm}^{-2}$ ), 3D-INCT ( $8.98 \text{ mF cm}^{-2}$ ) and 3D-ICT ( $5.6 \text{ mF cm}^{-2}$ ). The increased ECSA should originate from the high exposure of active sites owing to the 3D interconnected structures, and the enhanced mass transmission might also partly illuminate the apparent activity of NiSAs@3D-INCT [47]. The CO partial current densities of the different samples normalized by ECSA have also been considered. As depicted in Fig. S20, the ECSA-normalized  $j_{CO}$  of NiSAs@3D-INCT is still much higher than those of other reference samples, suggesting the better intrinsic activity of NiSAs@3D-INCT resulted from the existence of highly reactive Ni-N<sub>4</sub> sites [60]. To further figure out the kinetics of the CO<sub>2</sub>RR on NiSAs@3D-INCT, Tafel analysis was conducted (Fig. 3e). The NiSAs@3D-INCT has a much smaller Tafel slope of  $104 \text{ mV dec}^{-1}$  than that of 3D-INCT ( $230 \text{ mV dec}^{-1}$ ), implying that the first proton-coupled electron transfer to CO<sub>2</sub> to form a COOH\* intermediate on NiSAs@3D-INCT is rate-determining and faster due to the highly active Ni-N<sub>4</sub> moiety [61]. In addition, the NiNPs@3D-INCT shows a similar Tafel slope ( $110 \text{ mV dec}^{-1}$ ) with NiSAs@3D-INCT. As the synthesis of NiNPs@3D-INCT only lacks the acid leaching step compared with that of NiSAs@3D-INCT, it can be indicated that their intrinsic activities of CO<sub>2</sub>RR are derived from Ni-N<sub>4</sub> sites, and NiNPs can hardly be effective. Furthermore, the electrochemical impedance spectroscopy (EIS) results indicate that the NiSAs@3D-INCT has smaller charge transfer resistance than other samples (Fig. S21), further supporting the faster electron/mass transport and higher catalytic kinetics of NiSAs@3D-INCT. To optimize the catalytic performance, the loading Ni content of NiSAs@3D-INCT could be controlled by changing the concentration of Ni(NO<sub>3</sub>)<sub>2</sub> impregnation solution of 0.05 M and 0.5 M (see details in Fig. S22). Briefly, the NiSAs@3D-INCT obtained in 0.2 M Ni(NO<sub>3</sub>)<sub>2</sub> showed higher current density and selectivity than those of samples obtained in 0.05 M and 0.5 M Ni(NO<sub>3</sub>)<sub>2</sub>, indicating the CO<sub>2</sub>RR performance can be optimized by the loading Ni content.

The long-term CO<sub>2</sub> reduction stability measurements of the NiSAs@3D-INCT were operated at  $-0.69$  and  $-0.86$  V vs. RHE, respectively. The current density and the  $FE_{CO}$  both show a slight decay during the 12 h of uninterrupted operation (Fig. 3f and Fig. S23), verifying the good stability of NiSAs@3D-INCT. The XRD patterns show that there was no visible change of the diffraction peaks, indicating that the 3D-INCT has a good stability and durability in the stability test (Fig. S24a). The TEM image reveals that the NiSAs@3D-INCT maintained the structurally-integrated and interconnected carbon tube structure with no morphological changes during the stability test. Moreover, the AC-HAADF-STEM image shows that the Ni single atoms were still isolated and uniformly distributed without agglomeration, and no cluster and nanoparticle was found after stability test (Fig. S24b, c). The above electrocatalytic results obviously indicate that the superior

CO<sub>2</sub>RR performance of NiSAs@3D-INCT can be assigned to the interconnected tubular structure for facilitating the diffusion of CO<sub>2</sub> and electrolyte, as well as the existence of highly active atomically distributed Ni-N<sub>4</sub> sites.

### 3.3. Mechanism analyses

To gain theoretical insights of excellent electrocatalytic performance of the NiSAs@3D-INCT for CO<sub>2</sub>RR, the thermodynamic investigation such as Gibbs free energy must be conducted. The DFT computations were further performed to acquire the Gibbs free energy of different reaction intermediates, and three coordination structures, including Ni-N<sub>4</sub>-C (according to the result of EXAFS), N-C and Ni (111), were optimized as the models for calculations (Fig. S25). The Ni-N bond length in the model of Ni-N<sub>4</sub>-C is  $1.85 \text{ \AA}$ , which is compatible with the experimental value ( $1.88 \text{ \AA}$ ). Generally, the pathways of CO<sub>2</sub>RR to produce CO can be summarized as the following steps. 1) The adsorption of CO<sub>2</sub> at active sites (denoted as \*); 2) the protonation of CO<sub>2</sub> by the first proton-coupled electron transfer step to form COOH\* intermediate; 3) the conversion of COOH\* by the second proton-coupled electron step to generate the CO\* intermediate; 4) the desorption of the as-formed CO\* to produce CO (Fig. 4a) [27]. The Gibbs free energy changes of the above CO<sub>2</sub>RR pathways on Ni-N<sub>4</sub>-C, N-C and Ni (111) are showed in Fig. 4b. The rate-determining step (RDS) with the highest free energy barrier was found to be the formation of adsorbed COOH\* for both Ni-N<sub>4</sub>-C and N-C [62], in good agreement with the analysis of Tafel slope. The free energy change to form COOH\* on Ni-N<sub>4</sub>-C is calculated to be  $1.36 \text{ eV}$ , which is much lower than that on N-C ( $2.12 \text{ eV}$ ). This result indicates that the decoration of NiSAs with Ni-N<sub>4</sub> configuration reduces the formation energy of COOH\*, which could significantly facilitate the following formation of CO and thus remarkably promote the CO<sub>2</sub>RR activity. Although the Ni (111) has most favourable formation energy of \*COOH, the free energy change for CO desorption is highly endothermic ( $2.82 \text{ eV}$ ), indicating that the Ni (111) site can be easily poisoned by \*CO. As hydrogen evolution reaction (HER) is the main competition reaction, the free energy diagrams of CO<sub>2</sub>RR and HER on Ni-N<sub>4</sub>-C are also compared in Fig. 4c. Obviously, the free energy change for formation of COOH\* ( $1.36 \text{ eV}$ ) is lower than that of \*H ( $1.47 \text{ eV}$ ), indicating that the Ni-N<sub>4</sub> sites were preferentially occupied by the CO<sub>2</sub>RR rather than HER, which corresponds with the experiments [51]. The comparisons of free energy diagrams of CO<sub>2</sub>RR and HER on N-C and Ni (111) (Fig. S26) further demonstrate that the HER reaction is more likely to occur on the N-C and Ni (111) sites, which is consistent with the experimental results. Projected density of states (PDOS) values were calculated to further explore the electronic origin of the high catalytic activity at the Ni-N<sub>4</sub>-C site. As shown in Fig. S27, the calculated d-band center of the Ni 3d in Ni (111) is  $-1.27 \text{ eV}$ , which is much closer to the Fermi level compared with that of Ni-N<sub>4</sub>-C ( $-2.43 \text{ eV}$ ), indicating that the strong binding strength of CO\* would lead to the poisoning of the active centers in Ni (111) [63,64], which is corresponding to the highly positive energy of CO desorption calculated above. In addition, the PDOS of the atom (Ni in Ni-N<sub>4</sub>-C or N in N-C) bonded to intermediates (\*COOH/\*CO), as well as those of the group \*COOH/\*CO, are also calculated (Fig. 4d, e). The stronger hybridization between Ni and \*COOH than that between N and \*COOH demonstrates a stronger interaction between Ni and \*COOH, further indicating that Ni-N<sub>4</sub>-C promotes the CO<sub>2</sub>RR activity more easily [65]. Taken together these DFT calculations agree well with the above experimental results, and support further insights to explain the superior CO<sub>2</sub>RR activity and selectivity of NiSAs@3D-INCT.

## 4. Conclusions

In summary, we have rationally designed and constructed Ni single atoms supported on the 3D interconnected N-doped carbon tube (NiSAs@3D-INCT) network as a self-supported electrode for efficient

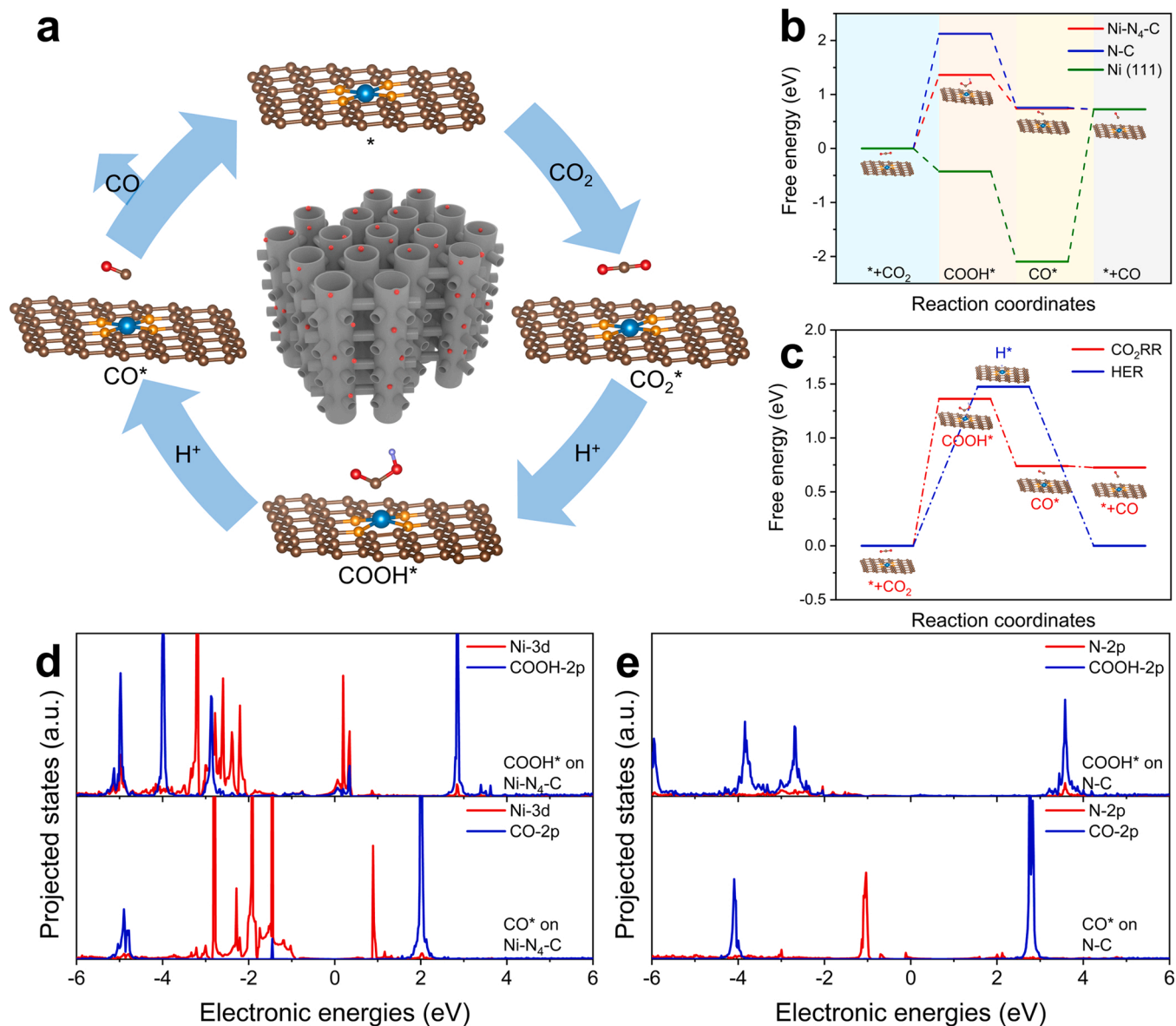


**Fig. 4.** a) The proposed reaction pathways for CO<sub>2</sub>RR on Ni-N<sub>4</sub>-C doped graphene. b) Free energy diagrams for CO<sub>2</sub>RR on Ni-N<sub>4</sub>-C, N-C doped graphene and Ni (111). c) Comparison of free energy diagrams for CO<sub>2</sub>RR and HER on the Ni-N<sub>4</sub>-C model. d) PDOS of adsorption structures of \*COOH and \*CO on Ni-N<sub>4</sub>-C. e) PDOS of adsorption structures of \*COOH and \*CO on N-C.

and stable CO<sub>2</sub>RR. Benefitting from the interconnected and hierarchical channels of the 3D-INCT support, a high density of atomically isolated Ni single atoms have been successfully loaded, which significantly enhance the intrinsic activity for CO<sub>2</sub>RR. Meanwhile, the unique interconnected tubular network structure of NiSAs@3D-INCT greatly promotes the excellent diffusion of CO<sub>2</sub> and transmission of electrolyte, as well as accelerates the electrocatalytic kinetics. The coupling effect of the high-density active sites and unhindered mass transmission has greatly improved the intrinsic and holistic activity of CO<sub>2</sub>RR on NiSAs@3D-INCT. As a result, the self-supported and binder-free NiSAs@3D-INCT electrode exhibits an excellent CO<sub>2</sub>RR activity and selectivity, with a large value of partial current density of 51.8 mA cm<sup>-2</sup> at -0.96 V vs. RHE and a high FE of 91.4% at -0.86 V vs. RHE for CO product. DFT calculations demonstrate that the atomic Ni-N<sub>4</sub> moiety is the highly active site in NiSAs@3D-INCT for CO<sub>2</sub>RR. This work would inspire the exploration of an alternative new way towards developing advanced SACs and self-supported electrodes for high-performance CO<sub>2</sub>RR.

#### CRediT authorship contribution statement

The manuscript was written through contributions of all authors. All authors have given approval to the final version of the manuscript. **K. W.**, **B.C.**, **Y.X.**, and **G.M.** conceived the idea and directed the project. **K. W.** designed the experiment, synthesized and characterized the samples, performed the electrochemical measurements, and drafted the manuscript. **W.F.** conducted XAS measurements and analysis. **N.S.** carried out the DFT calculations. **S.C.** discussed the study. **Y.X.** procured the research grants and supervised the project.

#### Declaration of Competing Interest

The authors declare that they have no known competing financial interests or personal relationships that could have appeared to influence the work reported in this paper.



## Data Availability

No data was used for the research described in the article.

## Acknowledgements

This work was financially supported by the Basic Science Center Program for Ordered Energy Conversion of the National Natural Science Foundation of China (No. 51888103), and the National Natural Science Foundation of China (No. 52102324, 91963202).

## Appendix A. Supporting information

Supplementary data associated with this article can be found in the online version at [doi:10.1016/j.apcatb.2023.123083](https://doi.org/10.1016/j.apcatb.2023.123083).

## References

- [1] T.N. Nguyen, M. Salehi, Q.V. Le, A. Seifitokaldani, C.T. Dinh, Fundamentals of electrochemical CO<sub>2</sub> reduction on single-metal-atom catalysts, *ACS Catal.* 10 (2020) 10068–10095.
- [2] Q. Zhu, Y. Xuan, K. Zhang, K. Chang, Enhancing photocatalytic CO<sub>2</sub> reduction performance of g-C<sub>3</sub>N<sub>4</sub>-based catalysts with non-noble plasmonic nanoparticles, *Appl. Catal. B Environ.* 297 (2021), 120440.
- [3] H. Feng, D. Liu, Y. Zhang, X.Y. Shi, O.C. Esan, Q. Li, R. Chen, L. An, Advances and challenges in photoelectrochemical redox batteries for solar energy conversion and storage, *Adv. Energy Mater.* 12 (2022), 2200469.
- [4] K. Gao, X. Liu, Z. Jiang, H. Zheng, C. Song, X. Wang, C. Tian, C. Dang, N. Sun, Y. Xuan, Direct solar thermochemical CO<sub>2</sub> splitting based on Ca- and Al-doped SmMnO<sub>3</sub> perovskites: ultrahigh CO yield within small temperature swing, *Renew. Energy* 194 (2022) 482–494.
- [5] B. Chen, D. Kim, Z. Zhang, M. Lee, K. Yong, MOF-derived NiCoZnP nanoclusters anchored on hierarchical N-doped carbon nanosheets array as bifunctional electrocatalysts for overall water splitting, *Chem. Eng. J.* 422 (2021), 130533.
- [6] W. Hua, H. Sun, L. Lin, Q. Mu, B. Yang, Y. Su, H. Wu, F. Lyu, J. Zhong, Z. Deng, Y. Peng, A hierarchical Single-Atom Ni-N<sub>3</sub>-C catalyst for electrochemical CO<sub>2</sub> reduction to CO with Near-Unity faradaic efficiency in a broad potential range, *Chem. Eng. J.* 446 (2022), 137296.
- [7] C. Wang, H. Ren, Z. Wang, Q. Guan, Y. Liu, W. Li, A promising single-atom Co-N-C catalyst for efficient CO<sub>2</sub> electroreduction and high-current solar conversion of CO<sub>2</sub> to CO, *Appl. Catal. B Environ.* 304 (2022), 120958.
- [8] H.B. Yang, S.-F. Hung, S. Liu, K. Yuan, S. Miao, L. Zhang, X. Huang, H.-Y. Wang, W. Cai, R. Chen, J. Gao, X. Yang, W. Chen, Y. Huang, H.M. Chen, C.M. Li, T. Zhang, B. Liu, Atomically dispersed Ni(i) as the active site for electrochemical CO<sub>2</sub> reduction, *Nat. Energy* 3 (2018) 140–147.
- [9] S. Chang, Y. Xuan, J. Duan, K. Zhang, High-performance electroreduction CO<sub>2</sub> to formate at Bi/Nafion interface, *Appl. Catal. B Environ.* 306 (2022), 121135.
- [10] S. Payra, S. Shenoy, C. Chakraborty, K. Tarafder, S. Roy, Structure-sensitive electrocatalytic reduction of CO<sub>2</sub> to methanol over carbon-supported intermetallic PtZn Nano-Alloys, *ACS Appl. Mater. Interfaces* 12 (2020) 19402–19414.
- [11] Y. Zhang, Q. Zhou, Z.F. Qiu, X.Y. Zhang, J.Q. Chen, Y. Zhao, F. Gong, W.Y. Sun, Tailoring coordination microenvironment of Cu(I) in metal-organic frameworks for enhancing electroreduction of CO<sub>2</sub> to CH<sub>4</sub>, *Adv. Funct. Mater.* 32 (2022), 2203677.
- [12] Z.Y. Yin, C. Yu, Z.L. Zhao, X.F. Guo, M.Q. Shen, N. Li, M. Muzzio, J.R. Li, H. Liu, H. H. Lin, J. Yin, G. Lu, D. Su, S.H. Sun, Cu<sub>2</sub>N nanocubes for selective electrochemical reduction of CO<sub>2</sub> to ethylene, *Nano Lett.* 19 (2019) 8658–8663.
- [13] D.L. Meng, M.D. Zhang, D.H. Si, M.J. Mao, Y. Hou, Y.B. Huang, R. Cao, Highly selective tandem electroreduction of CO<sub>2</sub> to ethylene over atomically isolated Nickel-Nitrogen site/copper nanoparticle catalysts, *Angew. Chem. Int. Ed.* 60 (2021) 25485–25492.
- [14] W. Xiong, D. Si, J. Yi, Y. Huang, H. Li, R. Cao, Morphology and composition dependence of multicomponent Cu-based nanoreactor for tandem electrocatalysis CO<sub>2</sub> reduction, *Appl. Catal. B Environ.* 314 (2022), 121498.
- [15] H. Han, Y. Noh, Y. Kim, S. Park, W. Yoon, D. Jang, S.M. Choi, W.B. Kim, Selective electrochemical CO<sub>2</sub> conversion to multicarbon alcohols on highly efficient N-doped porous carbon-supported Cu catalysts, *Green. Chem.* 22 (2020) 71–84.
- [16] H. Yang, Q. Lin, C. Zhang, X. Yu, Z. Cheng, G. Li, Q. Hu, X. Ren, Q. Zhang, J. Liu, C. He, Carbon dioxide electroreduction on single-atom nickel decorated carbon membranes with industry compatible current densities, *Nat. Commun.* 11 (2020) 593.
- [17] R. Daiyan, X. Tan, R. Chen, W.H. Saputera, H.A. Tahini, E. Lovell, Y.H. Ng, S. C. Smith, L.M. Dai, X.Y. Lu, R. Amal, Electroreduction of CO<sub>2</sub> to CO on a mesoporous carbon catalyst with progressively removed nitrogen moieties, *ACS Energy Lett.* 3 (2018) 2292–2298.
- [18] Z. Chen, G. Zhang, Y. Wen, N. Chen, W. Chen, T. Regier, J. Dynes, Y. Zheng, S. Sun, Atomically dispersed Fe-Co bimetallic catalysts for the promoted electroreduction of carbon dioxide, *Nanomicro Lett.* 14 (2021) 25.
- [19] S. Narayanaru, J. Chinnaiiah, K.L. Phani, F. Scholz, pH dependent CO adsorption and roughness-induced selectivity of CO<sub>2</sub> electroreduction on gold surfaces, *Electrochim. Acta* 264 (2018) 269–274.
- [20] X.Y. Shen, X.K. Liu, S.C. Wang, T. Chen, W. Zhang, L.L. Cao, T. Ding, Y. Lin, D. Liu, L. Wang, W. Zhang, T. Yao, Synergistic modulation at atomically dispersed Fe/Au interface for selective CO<sub>2</sub> electroreduction, *Nano Lett.* 21 (2021) 686–692.
- [21] S.B. Liu, C. Sun, J. Xiao, J.L. Luo, Unraveling structure sensitivity in CO<sub>2</sub> electroreduction to near-unity CO on silver nanocubes, *ACS Catal.* 10 (2020) 3158–3163.
- [22] H. Guo, D.-H. Si, H.-J. Zhu, Q.-X. Li, Y.-B. Huang, R. Cao, Ni single-atom sites supported on carbon aerogel for highly efficient electroreduction of carbon dioxide with industrial current densities, *eScience* 2 (2022) 295–303.
- [23] W. Ni, Z. Liu, Y. Zhang, C. Ma, H. Deng, S. Zhang, S. Wang, Electroreduction of carbon dioxide driven by the intrinsic defects in the carbon plane of a single Fe-N<sub>4</sub> site, *Adv. Mater.* 33 (2021), 2003238.
- [24] N. Mohd Adli, W. Shan, S. Hwang, W. Samarakoon, S. Karakalos, Y. Li, D.A. Cullen, D. Su, Z. Feng, G. Wang, G. Wu, Engineering atomically dispersed FeN<sub>4</sub> active sites for CO<sub>2</sub> electroreduction, *Angew. Chem. Int. Ed.* 60 (2021) 1022–1032.
- [25] X. Li, W. Bi, M. Chen, Y. Sun, H. Ju, W. Yan, J. Zhu, X. Wu, W. Chu, C. Wu, Y. Xie, Exclusive Ni-N<sub>4</sub> sites realize near-unity CO selectivity for electrochemical CO<sub>2</sub> reduction, *J. Am. Chem. Soc.* 139 (2017) 14889–14892.
- [26] Z. Chen, X. Zhang, W. Liu, M. Jiao, K. Mou, X. Zhang, L. Liu, Amination strategy to boost the CO<sub>2</sub> electroreduction current density of M-N/C single-atom catalysts to the industrial application level, *Energy Environ. Sci.* 14 (2021) 2349–2356.
- [27] X. Fu, P. Zhang, T. Sun, L. Xu, L. Gong, B. Chen, Q. Xu, T. Zheng, Z. Yu, X. Chen, S. Zhang, M. Hou, H. Wang, K. Wang, J. Jiang, Atomically dispersed Ni-N<sub>3</sub> sites on highly defective micro-mesoporous carbon for superior CO<sub>2</sub> electroreduction, *Small* 18 (2022), 2107997.
- [28] Y. Li, X.F. Lu, S. Xi, D. Luan, X. Wang, X.W.D. Lou, Synthesis of N-Doped highly graphitic carbon urchin-like hollow structures loaded with Single-Ni atoms towards efficient CO<sub>2</sub> electroreduction, *Angew. Chem. Int. Ed.* 61 (2022), e202201491.
- [29] Y.N. Gong, L. Jiao, Y.Y. Qian, C.Y. Pan, L.R. Zheng, X.C. Cai, B. Liu, S.H. Yu, H. L. Jiang, Regulating the coordination environment of MOF-templated single-atom nickel electrocatalysts for boosting CO<sub>2</sub> reduction, *Angew. Chem. Int. Ed.* 59 (2020) 2705–2709.
- [30] C. Wang, X. Hu, X. Hu, X. Liu, Q. Guan, R. Hao, Y. Liu, W. Li, Typical transition metal single-atom catalysts with a metal-pyridine N structure for efficient CO<sub>2</sub> electroreduction, *Appl. Catal. B Environ.* 296 (2021), 120331.
- [31] C. Zhang, S. Yang, J. Wu, M. Liu, S. Yazdli, M. Ren, J. Sha, J. Zhong, K. Nie, A. S. Jalilov, Z. Li, H. Li, B.I. Yakobson, Q. Wu, E. Ringe, H. Xu, P.M. Ajayan, J. M. Tour, Electrochemical CO<sub>2</sub> reduction with atomic iron-dispersed on nitrogen-doped graphene, *Adv. Energy Mater.* 8 (2018), 1703487.
- [32] Z. Li, R. Wu, S. Xiao, Y. Yang, L. Lai, J.S. Chen, Y. Chen, Axial chlorine coordinated iron-nitrogen-carbon single-atom catalysts for efficient electrochemical CO<sub>2</sub> reduction, *Chem. Eng. J.* 430 (2022), 132882.
- [33] H. Yang, Q. Lin, Y. Wu, G. Li, Q. Hu, X. Chai, X. Ren, Q. Zhang, J. Liu, C. He, Highly efficient utilization of single atoms via constructing 3D and free-standing electrodes for CO<sub>2</sub> reduction with ultrahigh current density, *Nano Energy* 70 (2020), 104454.
- [34] S. Li, M. Ceccato, X. Lu, S. Frank, N. Lock, A. Roldan, X.-M. Hu, T. Skrydstrup, K. Daasbjerg, Incorporation of nickel single atoms into carbon paper as self-standing electrocatalyst for CO<sub>2</sub> reduction, *J. Mater. Chem. A* 9 (2021) 1583–1592.
- [35] C. Zhao, Y. Wang, Z. Li, W. Chen, Q. Xu, D. He, D. Xi, Q. Zhang, T. Yuan, Y. Qu, J. Yang, F. Zhou, Z. Yang, X. Wang, J. Wang, J. Luo, Y. Li, H. Duan, Y. Wu, Y. Li, Solid-diffusion synthesis of single-atom catalysts directly from bulk metal for efficient CO<sub>2</sub> reduction, *Joule* 3 (2019) 584–594.
- [36] H.P. Yang, X.D. Wang, Q. Hu, X.Y. Chai, X.Z. Ren, Q.L. Zhang, J.H. Liu, C.X. He, Recent progress in self-supported catalysts for CO<sub>2</sub> electrochemical reduction, *Small Methods* 4 (2020), 1900826.
- [37] F.M. Han, O. Qian, G.W. Meng, D. Lin, G. Chen, S.P. Zhang, Q.J. Pan, X. Zhang, X. G. Zhu, B.Q. Wei, Structurally integrated 3D carbon tube grid-based high-performance filter capacitor, *Science* 377 (2022) 1004–1007.
- [38] B. Ravel, M. Newville, ATHENA, ARTEMIS, HEPHAESTUS: data analysis for X-ray absorption spectroscopy using IFFFIT, *J. Synchrotron Radiat.* 12 (2005) 537–541.
- [39] J.P. Perdew, K. Burke, M. Ernzerhof, Generalized gradient approximation made simple, *Phys. Rev. Lett.* 78 (1997), 1396–1396.
- [40] G. Kresse, D. Joubert, From ultrasoft pseudopotentials to the projector augmented-wave method, *Phys. Rev. B* 59 (1999) 1758–1775.
- [41] S. Grimme, J. Antony, S. Ehrlich, H. Krieg, A consistent and accurate ab initio parametrization of density functional dispersion correction (DFT-D) for the 94 elements H-Pu, *J. Chem. Phys.* 132 (2010), 154104.
- [42] Y. Guo, S. Yao, Y. Xue, X. Hu, H. Cui, Z. Zhou, Nickel single-atom catalysts intrinsically promoted by fast pyrolysis for selective electroreduction of CO<sub>2</sub> into CO, *Appl. Catal. B Environ.* 304 (2022), 120997.
- [43] X. Wang, S. Ding, T. Yue, Y. Zhu, M. Fang, X. Li, G. Xiao, Y. Zhu, L. Dai, Universal domino reaction strategy for mass production of single-atom metal-nitrogen catalysts for boosting CO<sub>2</sub> electroreduction, *Nano Energy* 82 (2021), 105689.
- [44] J. Zhang, H.L. Zou, Q. Qing, Y.L. Yang, Q.W. Li, Z.F. Liu, X.Y. Guo, Z.L. Du, Effect of chemical oxidation on the structure of single-walled carbon nanotubes, *J. Phys. Chem. B* 107 (2003) 3712–3718.
- [45] K.A. Wepasnick, B.A. Smith, K.E. Schrote, H.K. Wilson, S.R. Diegelmann, D. H. Fairbrother, Surface and structural characterization of multi-walled carbon nanotubes following different oxidative treatments, *Carbon* 49 (2011) 24–36.
- [46] G.X. Zhang, S.H. Sun, D.Q. Yang, J.P. Dodelet, E. Sacher, The surface analytical characterization of carbon fibers functionalized by H<sub>2</sub>SO<sub>4</sub>/HNO<sub>3</sub> treatment, *Carbon* 46 (2008) 196–205.

- [47] Y. Li, S.L. Zhang, W. Cheng, Y. Chen, D. Luan, S. Gao, X.W.D. Lou, Loading Single-Ni atoms on assembled hollow N-Rich carbon plates for efficient CO<sub>2</sub> electroreduction, *Adv. Mater.* 34 (2022), 2105204.
- [48] L. Zhong, C. Jiang, M. Zheng, X. Peng, T. Liu, S. Xi, X. Chi, Q. Zhang, L. Gu, S. Zhang, G. Shi, L. Zhang, K. Wu, Z. Chen, T. Li, M. Dahbi, J. Alami, K. Amine, J. Lu, Wood carbon based single-atom catalyst for rechargeable Zn–Air batteries, *ACS Energy Lett.* 6 (2021) 3624–3633.
- [49] S. Liang, Q. Jiang, Q. Wang, Y. Liu, Revealing the real role of nickel decorated nitrogen-doped carbon catalysts for electrochemical reduction of CO<sub>2</sub> to CO, *Adv. Energy Mater.* 11 (2021), 2101477.
- [50] Y. Zhang, L. Jiao, W. Yang, C. Xie, H.L. Jiang, Rational fabrication of low-coordinate single-atom Ni electrocatalysts by MOFs for highly selective CO<sub>2</sub> reduction, *Angew. Chem. Int. Ed.* 60 (2021) 7607–7611.
- [51] B. Chen, B. Li, Z. Tian, W. Liu, W. Liu, W. Sun, K. Wang, L. Chen, J. Jiang, Enhancement of mass transfer for facilitating industrial-level CO<sub>2</sub> electroreduction on atomic Ni–N<sub>4</sub> sites, *Adv. Energy Mater.* 11 (2021), 2102152.
- [52] Y. Lu, H. Wang, P. Yu, Y. Yuan, R. Shahbazian-Yassar, Y. Sheng, S. Wu, W. Tu, G. Liu, M. Kraft, R. Xu, Isolated Ni single atoms in nitrogen doped ultrathin porous carbon templated from porous g-C<sub>3</sub>N<sub>4</sub> for high-performance CO<sub>2</sub> reduction, *Nano Energy* 77 (2020), 105158.
- [53] C. Jia, S. Li, Y. Zhao, R.K. Hocking, W. Ren, X. Chen, Z. Su, W. Yang, Y. Wang, S. Zheng, F. Pan, C. Zhao, Nitrogen vacancy induced coordinative reconstruction of single-atom Ni catalyst for efficient electrochemical CO<sub>2</sub> reduction, *Adv. Funct. Mater.* 31 (2021), 2107072.
- [54] L. Jiao, W. Yang, G. Wan, R. Zhang, X. Zheng, H. Zhou, S.H. Yu, H.L. Jiang, Single-atom electrocatalysts from multivariate metal-organic frameworks for highly selective reduction of CO<sub>2</sub> at low pressures, *Angew. Chem. Int. Ed.* 59 (2020) 20589–20595.
- [55] L. Li, Z. Jiang, Y. Li, F. Li, Y. Pan, X. Zhang, Y. Liang, Z. Zheng, Regulating morphological features of nickel single-atom catalysts for selective and enhanced electroreduction of CO<sub>2</sub>, *Small Methods* 7 (2023), 2201213.
- [56] Y.N. Gong, C.Y. Cao, W.J. Shi, J.H. Zhang, J.H. Deng, T.B. Lu, D.C. Zhong, Modulating the electronic structures of dual-atom catalysts via coordination environment engineering for boosting CO<sub>2</sub> electroreduction, *Angew. Chem. Int. Ed.* 61 (2022), e202215187.
- [57] Y. Hou, Y. Liang, P. Shi, Y. Huang, R. Cao, Atomically dispersed Ni species on N-doped carbon nanotubes for electroreduction of CO<sub>2</sub> with nearly 100% CO selectivity, *Appl. Catal. B Environ.* 271 (2020), 118929.
- [58] R. Daiyan, X. Zhu, Z. Tong, L. Gong, A. Razmjou, R.-S. Liu, Z. Xia, X. Lu, L. Dai, R. Amal, Transforming active sites in nickel–nitrogen–carbon catalysts for efficient electrochemical CO<sub>2</sub> reduction to CO, *Nano Energy* 78 (2020), 105213.
- [59] W.-j. Wang, C. Cao, K. Wang, T. Zhou, Boosting CO<sub>2</sub> electroreduction to CO with abundant nickel single atom active sites, *Inorg. Chem. Front.* 8 (2021) 2542–2548.
- [60] H. Chang, H. Pan, F. Wang, Z. Zhang, Y. Kang, S. Min, Ni single atoms supported on hierarchically porous carbonized wood with highly active Ni–N<sub>4</sub> sites as a self-supported electrode for superior CO<sub>2</sub> electroreduction, *Nanoscale* 14 (2022) 10003–10008.
- [61] M. Liu, Y.J. Pang, B. Zhang, P. De Luna, O. Voznyy, J.X. Xu, X.L. Zheng, C.T. Dinh, F.J. Fan, C.H. Cao, F.P.G. de Arquer, T.S. Safaei, A. Mepham, A. Klinkova, E. Kumacheva, T. Filleter, D. Sinton, S.O. Kelley, E.H. Sargent, Enhanced electrocatalytic CO<sub>2</sub> reduction via field-induced reagent concentration, *Nature* 537 (2016) 382–386.
- [62] X. Yang, J. Cheng, B. Fang, X. Xuan, N. Liu, X. Yang, J. Zhou, Single Ni atoms with higher positive charges induced by hydroxyls for electrocatalytic CO<sub>2</sub> reduction, *Nanoscale* 12 (2020) 18437–18445.
- [63] M.-K. Hu, S. Zhou, D.-D. Ma, Q.-L. Zhu, New insight into heterointerfacial effect for heterogenized metallomacrocyclic catalysts in executing electrocatalytic CO<sub>2</sub> reduction, *Appl. Catal. B Environ.* 310 (2022), 121324.
- [64] H. Han, S. Jin, S. Park, M.H. Seo, W.B. Kim, Atomic iridium species anchored on porous carbon network support: An outstanding electrocatalyst for CO<sub>2</sub> conversion to CO, *Appl. Catal. B Environ.* 292 (2021), 120173.
- [65] C. Zhang, Z. Fu, Q. Zhao, Z. Du, R. Zhang, S. Li, Single-atom-Ni-decorated, nitrogen-doped carbon layers for efficient electrocatalytic CO<sub>2</sub> reduction reaction, *Electrochem Commun.* 116 (2020), 106758.